AIAA JOURNAL
Vol. 43, No. 1, January 2005

Nonlinear Aeroelastic Computations of a Wing/Pylon/Finned-Store Using Parallel Computing

Dong-Hyun Kim*
GyeongSang National University, Jinju 660-701, Republic of Korea
Young-Min Park†
Korea Aerospace Research Institute, Taejon 305-333, Republic of Korea
and
In Lee‡ and Oh Joon Kwon§
Korea Advanced Institute of Science and Technology, Taejon 305-701, Republic of Korea

Nonlinear aeroelastic computations are presented for a sweptback wing with underpylon/finned-store in the transonic and supersonic flow regions, where strong shock wave interactions exist. A modal-based coupled nonlinear aeroelastic analysis system with the matched-point concept has been developed using the high-speed parallel processing technique. Advanced numerical techniques such as computational structural dynamics and computational fluid dynamics are used. It is expected to provide accurate and useful engineering data in the aeroelastic and structural design of flight vehicles. For the nonlinear unsteady aerodynamics in high transonic flow region, Euler equations based on an unstructured grid system have been applied to consider fully the complex geometries. Linear and nonlinear aeroelastic computations have been conducted and are compared for the transonic and supersonic flow regions. Typically, it is shown that the advanced numerical approach gives much more conservative flutter boundary for the wing/pylon/store model than those predicted by the classical linear aerodynamic theories for high transonic flow. Also, important results indicate that in transonic flow the critical nonlinear flutter or limit-cycle oscillation-like phenomenon may be dominantly induced or within the bounds of strong possibility due to the shock coupling effect of unstable store induced vibration.

Introduction

GENERIC multipurpose military aircraft usually carry several types of wing-mounted external stores. Furthermore, loading an external store that includes a pylon connection part is the basic configuration of modern fighters. External stores can change the aerodynamic and aeroelastic characteristics of wings because of the aerodynamic, inertial, and elastic coupling effect with the wing. Some of the most difficult and most dangerous problems in aircraft aeroelasticity arise in the transonic flight regime. The difficulty stems from that the governing equations of transonic flow are inherently nonlinear, which has effectively precluded analytical solution by traditional approaches. Also, the danger arises because the transonic regime is often the most critical from a structural dynamic viewpoint. Nevertheless, the actual extent of the safety margins present in the design, such as the traditional flutter speed margin of 15–20% over a design dive-speed, cannot be demonstrated in flight tests because of either safety or performance limitations. It is essential, therefore, that accurate analysis methods, supported and verified by carefully conducted experimental procedures, form the cornerstone of the structural dynamicist's contribution to the process of designing transonic aircraft. With regard to these aspects, there is a practical need to develop a delicate computational analysis system based on the accurate theories such as computational fluid dynamics/computational structural dynamics (CFD/CSD), and it must be an essential and powerful tool to simulate effectively several complex flutter phenomena with various nonlinearities.

Since the 1980s, theoretical, numerical, and application studies of CFD/CSD-based aeroelastic analyses for clean wing models have been reported in Refs. 1–8. Those papers were based on several aerodynamic theories, such as transonic small disturbance (TSD), Euler, and Navier–Stokes codes. Recently, the parallel processing technique has become a most effective tool to reduce the huge wall clock time of accurate computational aeroelastic approaches. Alonso and Jameson[9] developed a two-dimensional parallel code that couples the solution of the Euler equations with the solution of the structural equations. Farhat et al.[10] suggested a family of mixed explicit/implicit staggered solution algorithms including some geometric conservation law problems. They also described the numerical investigations of effectiveness of some parallel coupling schemes. Byun and Guruswamy[11] developed a parallel version of the ENSAERO code, which was then used and extended by Goodwin et al.[12] Recently, Liu et al.[13] developed an integrated CFD/CSD simulation code for flutter calculations based on a parallel, multiblock, multigrid flow solver for the Euler/Navier–Stokes equations. Also, Bohbot et al.[14] demonstrated the damping properties of the flow viscosity on the flutter boundary using a parallel Navier–Stokes solver with the one-equation Spallart–Almaras turbulence model. Melville[15] conducted a practical nonlinear aeroelastic simulation for an F-16 fighter configuration in transonic flight. The inviscid parallelized Euler code based on the structured grid system was applied for numerical computations.

There have been some previous investigations of the effect of external stores on aeroelastic instability using relatively simple aerodynamic theories. Pollock et al.[16] presented the effect of slender store aerodynamics on wing/store flutter and the numerical method based on the doublet-lattice method and wind-tunnel data correction. Triplett[17] conducted linear flutter analyses for an F/A-18 wing with a tip store using the doublet-lattice method. Guruswamy et al.[18] effectively developed a computational method based on the ATRAN3S code and examined the influence of a tip store on transonic aeroelastic stability. Gern and Librescu[19] conducted efficiently work on the

Received 27 April 2002; accepted for publication 6 May 2004.

*Assistant Professor, School of Mechanical and Aerospace Engineering, 900 Gazwa, Gyeongnam. Member AIAA.
†Research Scientist, Aerodynamics Division, 45 Eocun-dong, Yusong-gu.
‡Professor, Department of Aerospace Engineering, 373-1 Yusong-gu. Senior Member AIAA.
§Associate Professor, Department of Aerospace Engineering, 373-1 Yusong-gu. Member AIAA.

static and the dynamic aeroelasticity of laminated composite wings carrying external stores. Various useful parametric studies have used efficient numerical methods. Also, Kim and Lee,[20,21] using a TSD code, conducted an investigation of the effect of underpylon/store aerodynamics and tip launcher and missile for a practical wing-box model in transonic and supersonic flows. It was shown that the tip store can make the wing aeroelastically unstable and even induce nonlinear limit-cycle oscillations.

Nowadays, accurate prediction of flutter boundary has becomes really important to reduce structural weight and to estimate actual flight performance in the design process. The main purposes of this paper are to develop a delicate and general computational analysis system and to consider exactly the effect of underpylon/store configurations. In this study, a modal-based numerical flutter analysis system in the time domain has been developed that includes the physical matched-point concept. Also, the full configurations including pylon/fined-store were completely considered. The parallel unstructured Euler solver (see Ref. 22) was adopted and newly modified to be coupled with the dynamic aeroelastic solver. Structural free vibration analyses have been performed using finite element method. Detailed nonlinear time responses are computed by the simultaneous coupled time-integration method in the transonic and supersonic flow regions. Various computational results are presented and investigated in detail.

Unsteady Aerodynamic Modeling

Governing Equations

The compressible Euler equations can be written in an integral form over a control volume V moving with a velocity $\boldsymbol{V}_g$,

$$\frac{\partial}{\partial t}\int_V \boldsymbol{Q}\,\mathrm{d}V + \oint_S F(\boldsymbol{Q})\cdot\boldsymbol{n}\,\mathrm{d}S = 0 \tag{1}$$

where

$$\boldsymbol{Q} = \begin{pmatrix} \rho \\ \rho u \\ \rho v \\ \rho w \\ e_0 \end{pmatrix}, \qquad F(\boldsymbol{Q},\boldsymbol{n}) = \begin{pmatrix} \rho\bar{u} \\ \rho u\bar{u} + pn_x \\ \rho v\bar{u} + pn_y \\ pw\bar{u} + pn_z \\ e_0\bar{u} + pV_n \end{pmatrix}$$

Also,

$$\bar{u} = \boldsymbol{n}\cdot(\boldsymbol{V}-\boldsymbol{V}_g), \qquad V_n = \boldsymbol{n}\cdot\boldsymbol{V}$$

where $\boldsymbol{V}_g$ and $\boldsymbol{n}$ are the grid velocity and the outward unit normal vector. Pressure and total enthalpy can be expressed from ideal gas relations:

$$p = (\gamma-1)\left[e_0 - \tfrac{1}{2}\rho(u^2+v^2+w^2)\right] \tag{2}$$

$$h = [\gamma/(\gamma-1)](p/\rho) + \tfrac{1}{2}\rho(u^2+v^2+w^2) \tag{3}$$

where γ is the specific ratio.

The inviscid flux across each cell face is computed by using Roe's flux-difference splitting formula.[23] For high-order spatial accuracy, the estimation of state variables at each cell face is achieved by interpolating the solution with a Taylor series expansion in the neighborhood of each cell center. The cell-averaged solution gradient required at the cell center for the preceding expansion is computed using the Gauss theorem by evaluating the surface integral for the closed surface of the tetrahedrons.

For unsteady computations, the governing equations can be differenced to include temporal numerical subiterations as a dual-time stepping. With the subiteration counter denoted by m, the solution vector $\boldsymbol{Q}$ at advancing time level $n+1$ is now defined as

$$\left[\left(\frac{V}{\Delta\tau^*}+\frac{3V}{2\Delta\tau}\right)I + \frac{\partial R}{\partial \boldsymbol{Q}}\right]^m \Delta\boldsymbol{Q}^m = -R^*(\boldsymbol{Q}^m) \tag{4}$$

where $\Delta\boldsymbol{Q}^m = \boldsymbol{Q}^{m+1} - \boldsymbol{Q}^m$. Also, τ^* denotes the pseudotime for dual-time stepping and $R^*(\boldsymbol{Q}^m)$ is the unsteady residual newly defined as

$$R^*(\boldsymbol{Q}^m) = R(\boldsymbol{Q}^m) + \frac{3\boldsymbol{Q}^m V^{n+1} - 4\boldsymbol{Q}^n V^n + \boldsymbol{Q}^{n-1}V^{n-1}}{2\Delta\tau} \tag{5}$$

The solution vector $\Delta\boldsymbol{Q}$ denotes the change in state variables between numerical subiterations during a certain time step. When the subiterations drive the residual toward zero, not only second-order time accuracy is achieved, but the linearization errors are also driven to zero. In this study, the Gauss–Seidel relaxation method is effectively used to solve iteratively the system of flow equations.

Furthermore, to avoid numerical errors induced by the deforming or moving mesh, the cell volumes are integrated forward in time adopting the geometric conservation law (GCL). The GCL used in this study is of the same integral form as the mass conservation law and defined by

$$\frac{\partial}{\partial\tau}\int_\Omega \mathrm{d}V - \oint_{\partial\Omega} V_g\cdot\boldsymbol{n}\,\mathrm{d}\Omega = 0 \tag{6}$$

Discretization of Eq. (7) yields

$$V_i^{n+1} = V_i^n + \Delta\tau\sum V_g\cdot\boldsymbol{n} \tag{7}$$

The local cell volumes at time level $(n+1)$ in Eq. (5) are computed to satisfy the GCL by applying the preceding equation at every global time step.

Parallel Implementation of the Solver

Parallelization of the Gauss–Seidel implicit scheme is fairly straightforward and has been well described in the literature.[24] The present flow solver is parallelized by partitioning the global computational domain into local subdomains. The intermediate decomposition or partitioning is performed using the MeTiS library.[25] The local-domain mesh data are allocated on each processor, and the calculation is performed on the local computational domain by updating the solution information among subdomain boundaries. The interboundaries commonly included in each subdomain are considered as artificial boundaries for data communication. To do this, ghost cells attached to these interboundaries for the present cell-centered scheme were also introduced. Initially, face-center values of the flow variables are interchanged through the interboundary faces. These values are used to calculate the flux Jacobian on the interboundary. Data communication among processors is achieved using the standard message-passing interface (MPI) library installed on a LINUX operating system. Next, the cell-center values are exchanged across the boundary during the Gauss–Seidel iteration (GSI). Boundary node values and the weighting factors for Laplacian averaging are also communicated to achieve the high-order reconstruction. In the present study, cell data are exchanged in each GSI, and face and node data are transferred for the next global iteration. Because 25–30 numerical iterations are typically required in each time step to obtain the local converged solution, much communication time is spent during the GSI process. Therefore, three or five times of actual communication are generally performed to reduce the communicational overhead due to the GSI. The details of fundamental aerodynamic theories and numerical validations can be found in Ref. 22.

Modified Spring Analogy for Robust Moving Grid

For analyses of complex moving body problems, a modified type of the spring analogy[26] is used to compute the deformation of the mesh during the time integration of the fluid. In the spring analogy, the mesh is considered as fictitious springs. Boundary nodes are to be moved by aeroelastic computations, and interior nodes are moved by the spring analogy with several iterations. In the present research, the segment spring method proposed by Batina[27] is basically adopted. Here, the equilibrium lengths of the springs are equal to the initial lengths of the segments.

At static equilibriums of the spring system, the forces at every node i have to be zero. The iterative equation can be expressed as

$$\boldsymbol{\delta}_i^{k+1} = \sum_{j=1}^{v_j} \alpha_{ij}\boldsymbol{\delta}_j^k \Big/ \sum_{j=1}^{v_j} \alpha_{ij} \tag{8}$$

where $\boldsymbol{\delta}_i = \Delta x_i \boldsymbol{i} + \Delta y_i \boldsymbol{j} + \Delta z_i \boldsymbol{k}$ and α_{ij} are the moving displacement of node i and the spring stiffness of node i connected to node j, respectively. The spring stiffness was classically considered as being inversely proportional to the segment lengths of each cell. This simple treatment of the spring network may often cause a major numerical instability because of the wrong regeneration of the grid for a complex geometry. Thus, in the present method, the nearest distance from the surface boundary is additionally considered to minimize the deformation of grids near the surface boundary as presented in Ref. 28:

$$\alpha_{ij} = 1 \Big/ d_i^m \sqrt{(x_i - x_j)^2 + (y_i - y_j)^2 + (z_i - z_j)^2} \tag{9}$$

where d_i is the nearest distance from the moving boundary surface and m is a user-defined number to control the rigidity of near-body cells. In this study, the order of m is assumed as 2–3 because it is sufficient to keep the numerical stability for the problems considered herein. The present method distributes stiffness quantities among springs in such a way that the value is a maximum for the spring attached to the moving boundaries and is gradually diminished as the distance from the boundaries increases. In addition, the present method is much more cost effective for large three-dimensional unsteady problems with moving boundaries because of much less required communication data and memory size. This simple treatment of the spring network may often cause a major numerical instability because of the highly skewed small cells near surface boundary. Basically, the small cells near the surface boundary cannot endure large deformation of the surface boundary. Thus, in the present method, the nearest distance from the surface boundary is additionally considered to add weights to the spring stiffness near the surface boundaries, as presented in Ref. 28. In this way, the major portion of grid deformations can be derived away from the surface boundaries, whereas the small cells near surface boundaries can maintain the nearly previous shapes with small deformations.

The grid distance information is computed only once during the preprocessing step of the domain decomposition process for parallel computing on the whole grid system. The original interdomain grids are finally moved by adding the final displacements obtained from the iterative numerical solution of Eq. (8):

$$\boldsymbol{x}_i^{\text{new}} = \boldsymbol{x}_i^{\text{old}} + \boldsymbol{\delta}_i^{k+1,\,\text{final}} \tag{10}$$

Note that because the present moving grid technique coupled with parallel processing is applied locally on each processor, disagreements of nodes at the communication boundaries occur due to the independent local applications of the spring analogy. To avoid this kind of nonsynchronization problem, coordinates of nodes at the communication boundaries also have to be transferred into each other as the numerical constraints.

Computational Aeroelastic Analysis

The governing aeroelastic equations of motion of a flexible wing are obtained by using the Rayleigh–Ritz method. In this method, the resulting aeroelastic displacement at any time can be expressed as a function of a finite set of selected modes. The general motion of the wing can be described by the separation of time and space variables as follows:

$$\{u(t)\} = [\Psi_x(x, y, z)]\{q(t)\}, \qquad \{v(t)\} = [\Psi_y(x, y, z)]\{q(t)\}$$
$$\{w(t)\} = [\Psi_z(x, y, z)]\{q(t)\} \tag{11}$$

where $\{u\}$, $\{v\}$, and $\{w\}$ are the structural deflections and $[\psi_x]$, $[\psi_y]$, and $[\psi_z]$ are the matrices of x-, y-, and z-direction displacements of the natural vibration modes. Usually, the number of columns for the modal matrix $[\psi]$ directly depends on the selection by consideration of natural mode used in the coupled aeroelastic analysis.

The aeroelastic equations of motion for an elastic wing are formulated in terms of generalized displacement response vector $\{q(t)\}$, which is a solution of

$$[M_g]\{\ddot{q}(t)\} + [C_g]\{\dot{q}(t)\} + [K_g]\{q(t)\} = \{F_g(t, q, \dot{q})\} \tag{12}$$

where t is the physical time, $[M_g]$ is the generalized mass matrix, $[C_g]$ is the generalized damping matrix, $[K_g]$ is the generalized stiffness matrix, and $\{F_g\}$ is the vector of generalized aerodynamic forces computed by integrating the pressure distributions on the wing surface as

$$F_{g_i} = \frac{1}{2}\rho U^2 c_r^2 \iint_S -C_p(x, y, z, t)(\boldsymbol{n}_x\psi_{xi} + \boldsymbol{n}_y\psi_{yi} + \boldsymbol{n}_z\psi_{zi})\frac{\mathrm{d}S}{c_r^2} \tag{13}$$

where ρ is the freestream air density, U is the freestream velocity, c_r is the reference chord length, S is the wing area, C_p is the unsteady pressure coefficient on the arbitrary wing surface, $\boldsymbol{n}_x$, $\boldsymbol{n}_y$, and $\boldsymbol{n}_z$ are the surface normal vectors for the x, y, and z directions, respectively, and ψ_i are the ith natural mode shape vectors interpolated on the aerodynamic surface mesh. The generalized aerodynamic forces of Eq. (13) are integrated numerically on the wing, pylon, and store surfaces.

In general, the computation time needed to solve the structural equation is much less than that required for the decomposed fluid domains. Thus, for the parallel coupling with the unsteady fluid domains, one single computer node is usually prepared to solve the structural equations. At each global time step, all of the local generalized forces computed from each computer node are to be transferred into the structural dynamic solver. Then, the generalized displacements can be obtained by solving the generalized structural dynamic equations. Next, the transformed physical displacements data for moving boundaries are to be transferred into each corresponding computer nodes for spring analogy and unsteady fluid solution. Data communications among computer nodes are also conducted using the standard MPI library installed on a LINUX operating system. In addition, this includes the staggered coupling algorithm with internal iterations to increase the temporal coupling accuracy. In this study, the time-marching process of the structure–fluid coupling was performed by similarly adopting the second-order staggered algorithm used in Ref. 29. It was known that this algorithm is constructed as a leap-frog scheme, where the fluid subsystem is always computed at half-time stations, whereas the structure subsystem is always computed at full-time stations. A road map of the temporal coupling process applied in this study is shown in Fig. 1. Here, the transferred structural displacement and velocity are to be normalized to maintain numerical consistency with the normalized fluid domain.

When state vector $\{x\}$ is introduced to perform efficiently the numerical integration, Eq. (12) can be recast into first-order form as

$$\{\dot{x}(t)\} = [A]\{x(t)\} + [B]\{\Gamma(t)\} \tag{14}$$

where

$$[A] = \begin{bmatrix} [0] & [I] \\ -[M_g]^{-1}[K_g] & -[M_g]^{-1}[C_g] \end{bmatrix}, \qquad [B] = \begin{bmatrix} [0] \\ [M_g]^{-1} \end{bmatrix}$$

$$\{x(t)\} = \begin{Bmatrix} \{q(t)\} \\ \{\dot{q}(t)\} \end{Bmatrix}, \qquad \{\Gamma(t)\} = \begin{Bmatrix} \{0\} \\ \{F_g(t)\} \end{Bmatrix}$$

For nonlinear structural systems, a typical numerical technique such as the Runge–Kutta method is commonly used, and for linear structural systems, we can use more efficient approaches. One of the most useful and fast techniques for linear system analysis can be derived from the assumption of setting the external force during a

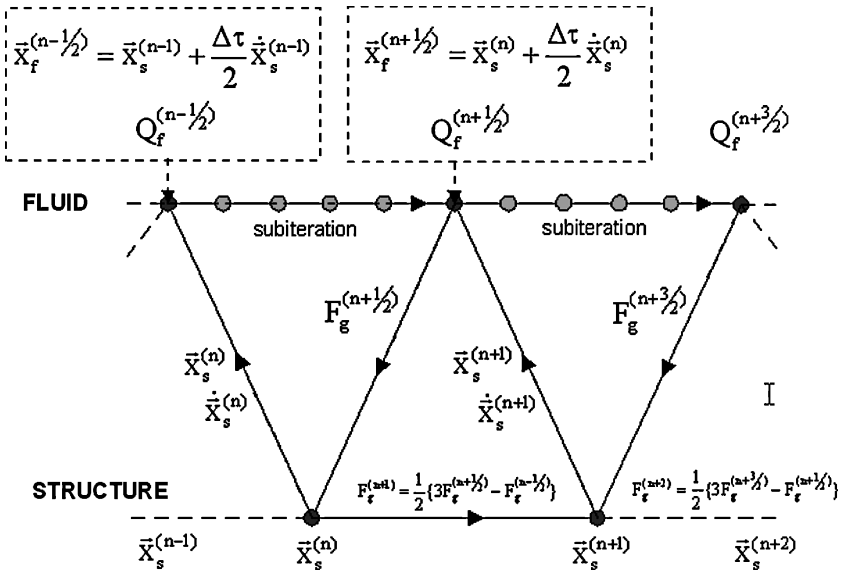

Fig. 1 Computation process of the second-order time-accurate staggered procedure.

certain small interval of the time-marching process. Thus, we can use the accurate analytical form of the solution obtained through the Laplace transform and inverse transform processes as

$$\{x(t)\} = e^{[A]t}\{x(0)\} + \int_0^t e^{[A](t-\tau)}[B]\{\Gamma(\tau)\}\,\mathrm{d}\tau \qquad (15)$$

The solution of Eq. (15) can be obtained numerically by replacing the continuous system by a discrete-time system. When a computational time interval is considered so that $n\Delta t < t \le (n+1)\Delta t$, and through the useful matrix manipulation for the integration of transition matrix, Eq. (15) can be derived as the following closed form:

$$\{x\}^{n+1} = e^{[A]\Delta t}\{x\}^n + [A]^{-1}(e^{[A]\Delta t} - I)[B]\{\Gamma\}^n \qquad (16)$$

From now on, Eq. (16) can be effectively integrated in time to predict the modal displacement and velocity using a digital computer as the following modified equation:

$$\{x\}^{n+1} = [\Phi]\{x\}^n + \tfrac{1}{2}[\Theta][B](3\{\Gamma\}^n - \{\Gamma\}^{n-1}) \qquad (17)$$

where

$$[\Phi] = e^{[A]\Delta t}, \qquad [\Theta] = [A]^{-1}(e^{[A]\Delta t} - I)$$

Note that the elements of the Φ and Θ matrices are dependent only on the values of time-step size and structural matrices $[M_g]$, $[C_g]$, and $[K_g]$. The detailed numerical method for Eq. (17) may be found in Ref. 30.

Surface Spline Techniques

The computed natural vibration mode shapes for a wing with pylon/store model are interpolated into the aerodynamic grid points using the surface spline methods. Using the surface spline method can map the structural model into the aerodynamic grid. By the application of the principle of virtual work, the relations between the finite element node and the aerodynamic grid points can be defined to interconnect each other. In this study, the numerical interpolations for the wing and the pylon parts are carried out by the infinite-plate spline because of its numerical smoothness and robustness. For the external stores with fins, the method based on the beam deflection theory is simply used because of its axisymmetric shape. As mentioned before, the store is assumed as a nearly rigid-beam structure with concentrated mass located at the c.g. point. This is straightforward and practical because the bending stiffness of the store body is relatively very high compared with those of the wing and pylon structures. In addition, applying a superposition technique with or

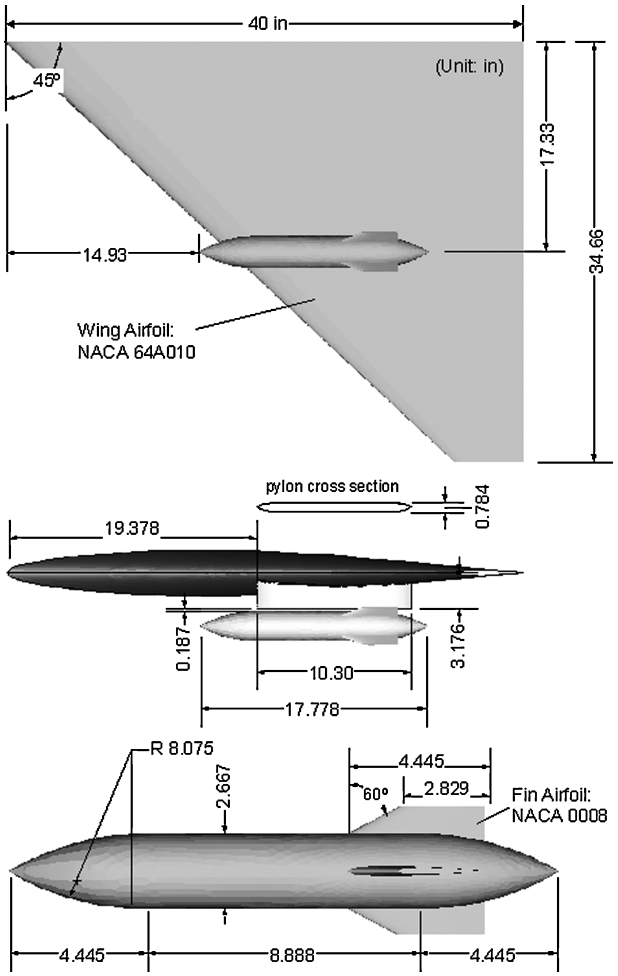

Fig. 2 Geometric configuration of a wing with pylon and finned-store.

without overlapping regions is basically useful in considering the complex shapes of flight vehicle structures that can be also decomposed as multicomponents. Enforcing the overlapping region can increase continuity at the decomposed structural boundaries. After performing surface splines for each structural component, these can be simply assembled into the original global configuration. The global free vibration modes interpolated on the aerodynamic surface mesh can be effectively displayed by the postcombination

process using a plotting program. Recent useful information for several spline techniques with numerical experiments may be found in Refs. 31 and 32.

Results and Discussion

The validation results of the present aeroelastic computation for the benchmark model of AGARD standard aeroelastic configuration (weakened 445.6) may be found in Ref. 30. Computational unstructured grids used in this study were generated by an in-house code and also the GAMBIT, which is a GUI-based grid- (structured and unstructured) generation module embedded in FLUENT (version 5.5) software. Figure 2 shows the geometric configurations of the present wing/pylon/finned-store model. Figure 3 shows an example of the unstructured surface grid generated by GAMBIT. The irregular bold lines indicate the communication boundaries decomposed for parallel computation. The full domain grid consists of 146,748 tetrahedral cells and 30,642 nodes. The surface boundaries on the wing, pylon, and store include 19,880 surface triangles and 10,035 nodes. Grid resolution is enforced at the leading edge, trailing edges, and tip of the main wing and store noses and fins. Far-field boundaries are located at about 10-chord lengths from the wing surface. The global mesh is usually decomposed as 20–24 subdomains using the MeTiS library (version 4.0). All of the computations were effectively carried out on a personal computer-clustered parallel machine with LINUX operating system. Steady aerodynamic flows are computed basically to investigate the shock interference effects. Mach numbers assumed for the present calculation are 0.95 and 1.2 at $\alpha = 0$ deg. Figure 4 shows the surface pressure distributions on the upper and lower wing surface interfering with the pylon and store at Mach 0.95 and 1.2. In Fig. 4, we can see the clear normal shock waves and strong interference effects between the lower wing surface and the pylon/store. Also, additional aerodynamic results for

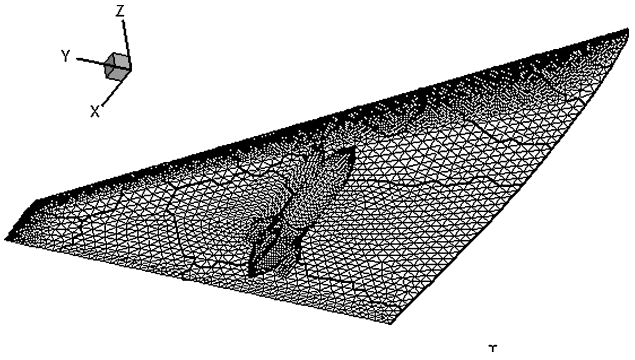

Fig. 3 Unstructured surface mesh of the wing with pylon/finned-store.

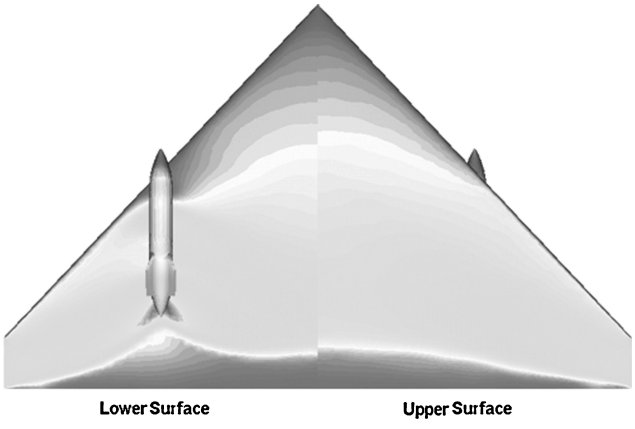

a) $M = 0.95$, $\alpha = 0.0$ deg

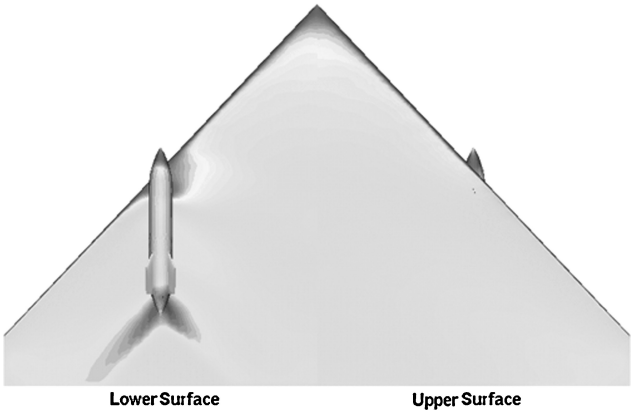

b) $M = 1.2$, $\alpha = 0.0$ deg

Fig. 4 Steady pressure contour of wing/pylon/finned-store model, $M = 0.95$ and 1.2.

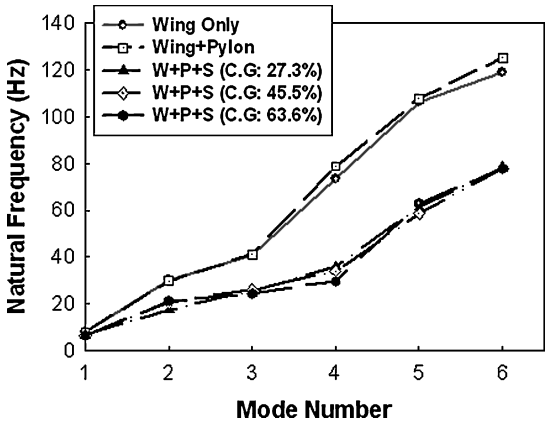

Fig. 5 Comparison of natural vibration frequencies of the wing/pylon/store model.

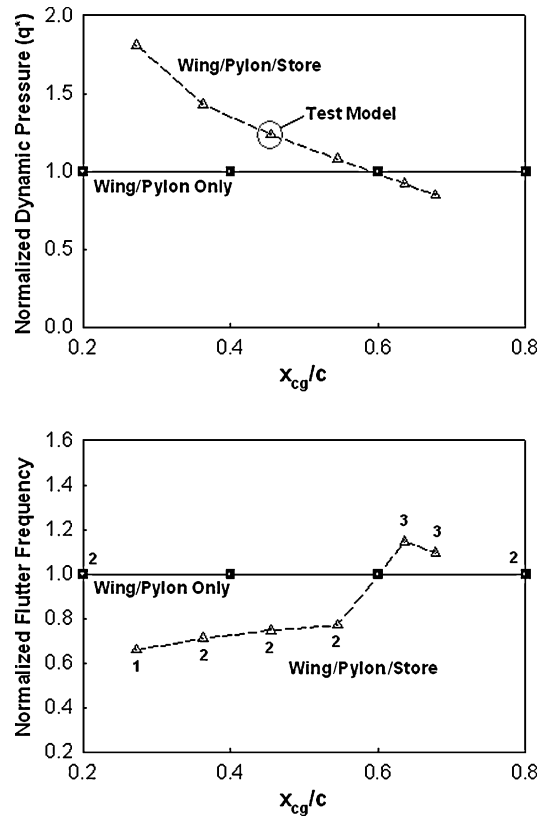

Fig. 6 Comparison of flutter dynamic pressure and frequency due to variation of store c.g location at $M = 0.6$.

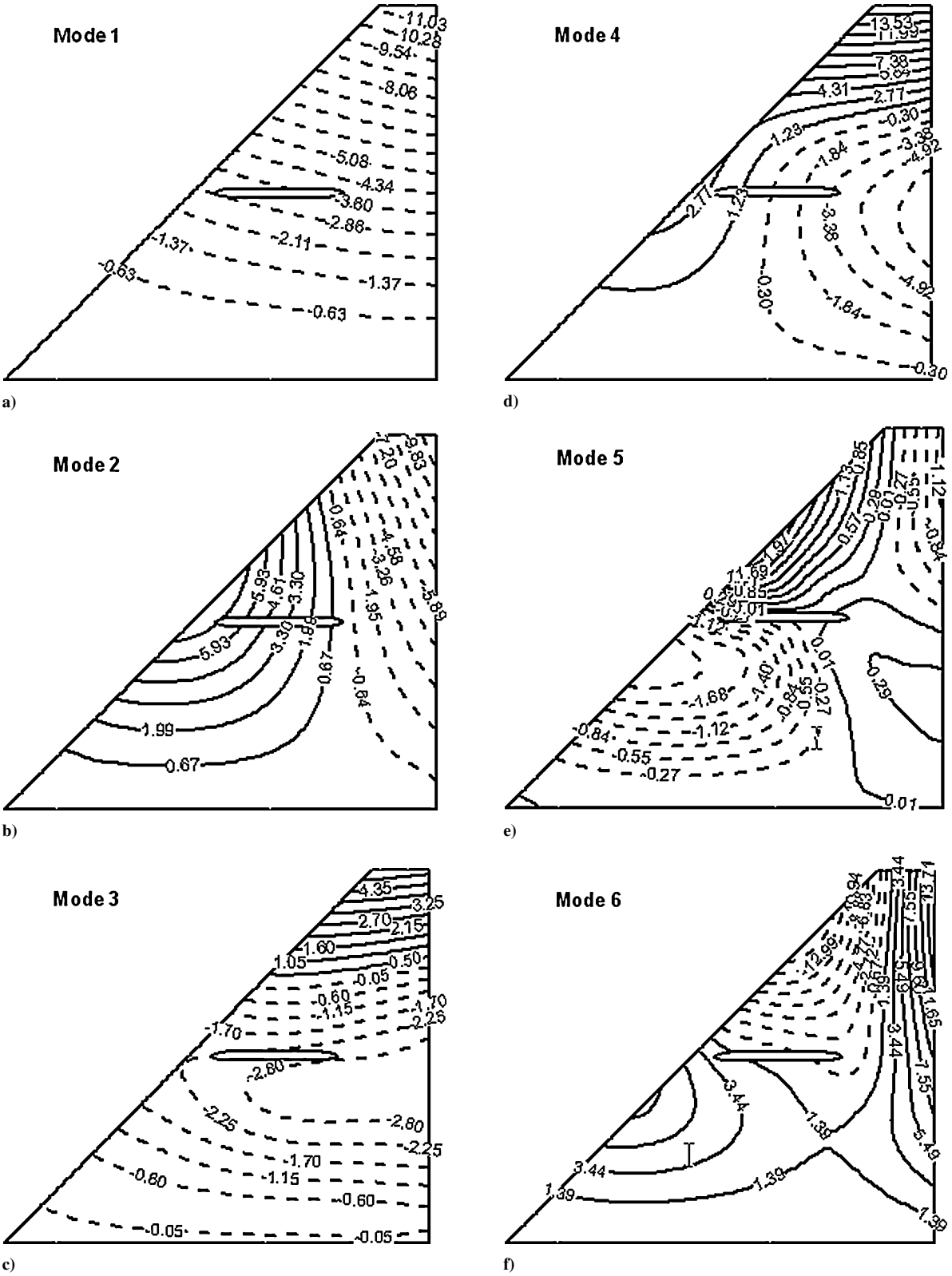

Fig. 7 Contour plot of free vibration mode shapes for model with 45.5% store c.g point.

steady and unsteady flows for the wing/pylon/pinned-store model may be found in Ref. 30.

A finite element model for the wing with a pylon-store model was created and structural vibration analyses were performed by the MSC/NASTRAN (version 70.5) finite element program. The finite element model consists of the quadrilateral (CQUAD4) plate, the beam (CBAR), the concentrated mass (CONM2) with mass moment of inertias, and the rigid-link (RBAR) elements. In this study, the wing and the pylon are modeled as the plate elements. For academic clearance, the pylon was perfectly attached to the wing structure. The store body is modeled as the equivalent beam with nearly rigid stiffness. The material of the wing and pylon structure is considered as aluminum alloy with properties $E = 10.5 \times 10^6$ psi (72.39 GPa), $\nu = 0.33$, and $\rho_s = 2.588 \times 10^{-4}$ lbf $\cdot$ s^2/in.^{4} (2765.8 kg/m^3). The wing is cantilevered and fixed at its root. The weight and mass moment of inertia of the store are considered a concentrated mass

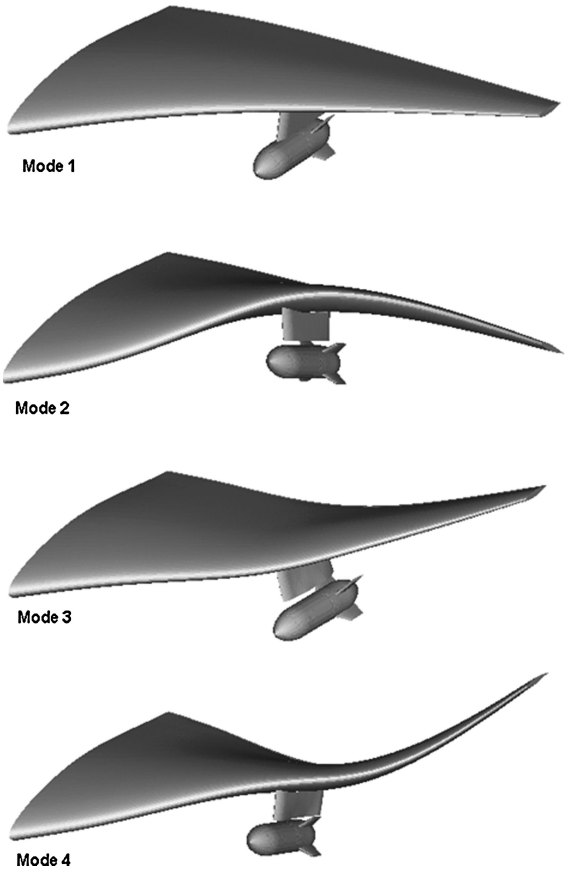

Fig. 8 Three-dimensional view of interpolated free vibration mode shapes.

element at the center of gravity. The structural connections between the pylon and the store were modeled as a rigid-link element at two nodes. The store weight is assumed as about 50% of the wing structural weight. In this case, the mass moment of inertia (MOI) of the store is $I_{yy} = I_{zz} = 0.2968$ lbf $\cdot$ s^2 $\cdot$ in. The MOI effect for the x axis is negligible for this axisymmetic store case.

Comparison of the lowest six natural frequencies is presented in Fig. 5. In the case of wing with pylon/store, the natural frequencies tend to be decreased because of the inertia effect of additional store mass. The changes of each natural frequency due to store locations seem to be small for the present model. To investigate the effect of store c.g. location on the flutter instability, linear flutter analyses have been conducted using a subsonic doublet-lattice and supersonic doublet-point aerodynamics, and then the solutions were obtained by applying the p–k method with the matched-point concept.[33] Figure 6 shows the comparison of normalized flutter dynamic pressure and frequency at Mach 0.6. It basically shows that the store location can significantly affect the flutter stability of the wing structure. From this investigation, the 45.5% c.g. location model is selected as a benchmark model for further study. Both six and eight natural modes were used in this analysis, and they give nearly similar flutter solutions for the present model.

Figure 7 shows the contour plots of the first six natural vibration modes for the model with 45.5% store mass center. Figure 8 shows the three-dimensional view of the interpolated modes for nonlinear Euler-based analysis. Here, the first mode is a pure bending, the second is a store pitch coupled bending/torsion mode, and the third is second bending with pylon bending and so on. In this study, the second mode is the major observed one in view of the critical store coupled flutter phenomenon in the high transonic flow region. Figures 9a and 9b show the $V-g$ and $V-f$ diagrams of the 45.5% c.g. location model at Mach 0.6 and 1.4, respectively. For subsonic flow, mode 2 is a dominant flutter mode, but for supersonic flow,

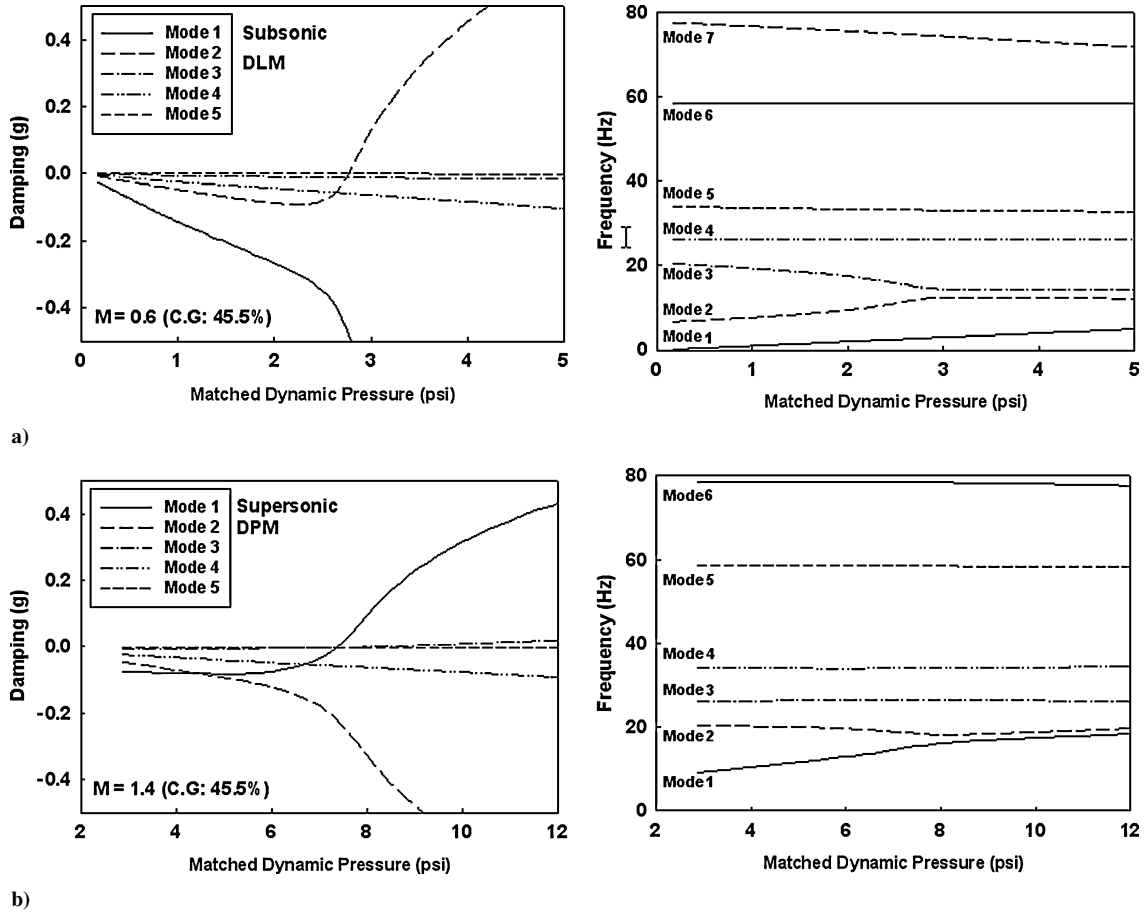

Fig. 9 V–g and V–f plots for the wing/pylon/store model with 45.5% store c.g location: a) $M = 0.6$ and b) $M = 1.4$.

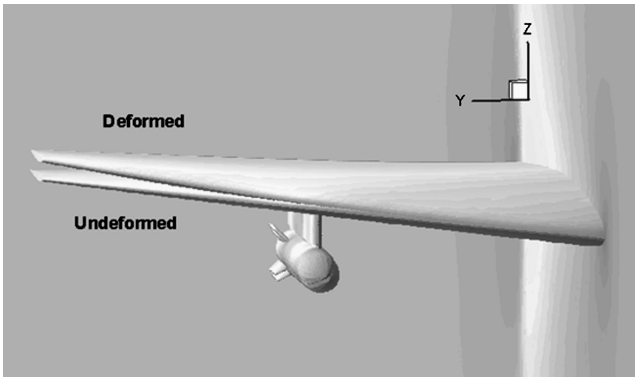

a)

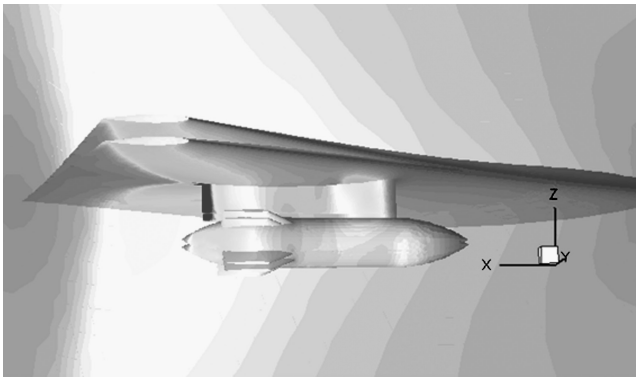

b)

Fig. 10 Three-dimensional views of a static wing deflection at Mach 0.95 and $\alpha_0 = 2.0$ deg.

mode 1 is a dominant one. The nonlinear flutter analysis using the coupled time-integration method includes the solution of static aeroelastic deflections for the nonzero steady lifting conditions. Figure 10 shows the three-dimensional view of static deflections due to the pressure loads under the flow conditions of $M = 0.9$ and $\alpha = 2$ deg. Here, we can clearly see the deformation of wing with some wash-out effect at the wing tip.

Figure 11 shows the lowest four computed generalized displacements at the given dynamic pressures for several Mach numbers. The total number of natural modes used for this computation is six. For $M = 0.6$, the dominant unstable flutter modes can be considered as the first and second mode in this case. The first modal velocity was enforced as an initial condition. For $M = 1.2$, the first mode response is still dominant compared to the other modal responses. This trend can be also observed in the frequency-domain solutions of Fig. 9. For $M = 0.95$, note that the flutter is rapidly induced by the second natural mode. From 1.0 s, we can see that the second mode has already become unstable, although the first mode still shows a stable response. As shown in Figs. 7 and 8, the second natural mode can be considered as a store pitch coupled (or induced) wing torsion dominant mode. Although not presented in this paper, no similar unstable responses for the clean wing model were observed. Thus, this unstable phenomenon can be considered as a typical store-induced flutter in the high transonic flow region.

The physical aeroelastic static and dynamic responses at the wing tip and the store nose near the flutter dynamic pressure are shown in Fig. 12. We can see the negative static deflection for subtransonic flow and the positive deflection for low-supersonic flow even at zero angle of attack. If there are no aerodynamic interference effects between the wing and the under-pylon/store, no static aeroelastic deflections of the wing are expected at zero angle of attack because the wing section is a symmetric airfoil. Note that static deflection indirectly can determine the amount of aerointerference effect and that the directions of static deflections for subsonic and

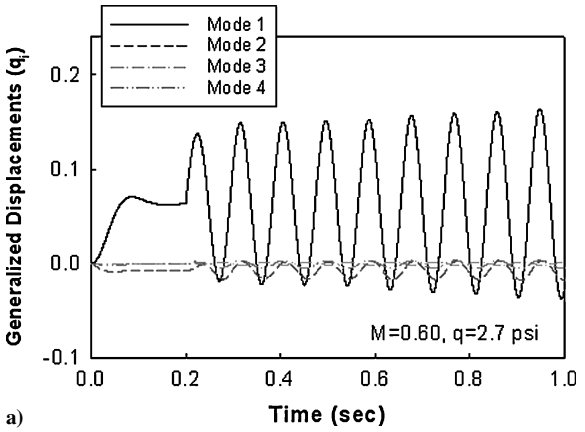

a)

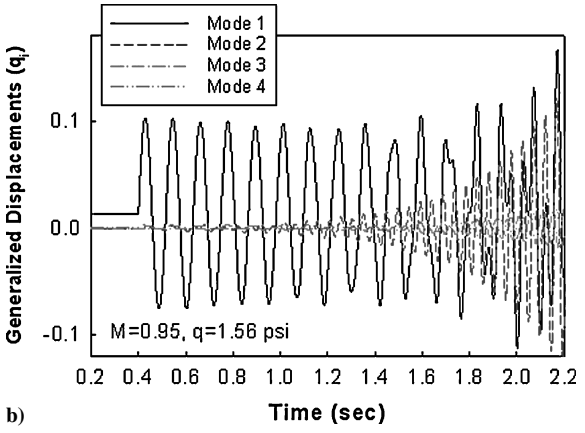

b)

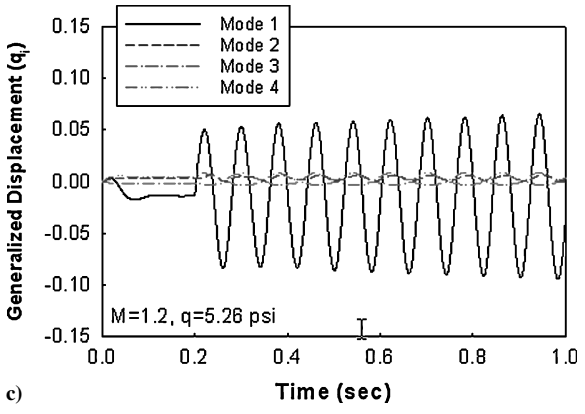

c)

Fig. 11 First four aeroelastic modal responses: a) $M = 0.6$, b) $M = 0.95$, and c) $M = 1.2$.

supersonic Mach numbers are opposite, as shown in Fig. 12. Because the first modal velocity is enforced as an initial condition, the generalized displacements of the first mode are dominantly shown for the cases of $M = 0.6$ and $M = 1.2$. However, an unusual result for $M = 0.95$ is the dominancy of the first modal response shown for the first-half of the time response. Then strong instability of the second mode due to wing/store aerodynamic interactions appeared for the latter-half of the response (Fig. 11). This is an important indication that there can be transition instabilities derived by nonlinear store-induced vibrations. After 1.0 s, we can observe unusual vibration patterns between lateral (U_y) and normal (U_z) displacements of the store nose. This result suggests that store-induced unstable motion due to shock wave interactions can be a major region for the global unstable vibration of the wing including limit-cycle oscillations. Classical fast Fourier transform was used, and the autospectral density functions of the aeroelastic responses are shown in Figs. 13 and 14 for each case. For $M = 0.6$ and $M = 1.2$, the resonance flutter frequency shows one value for both the wing tip

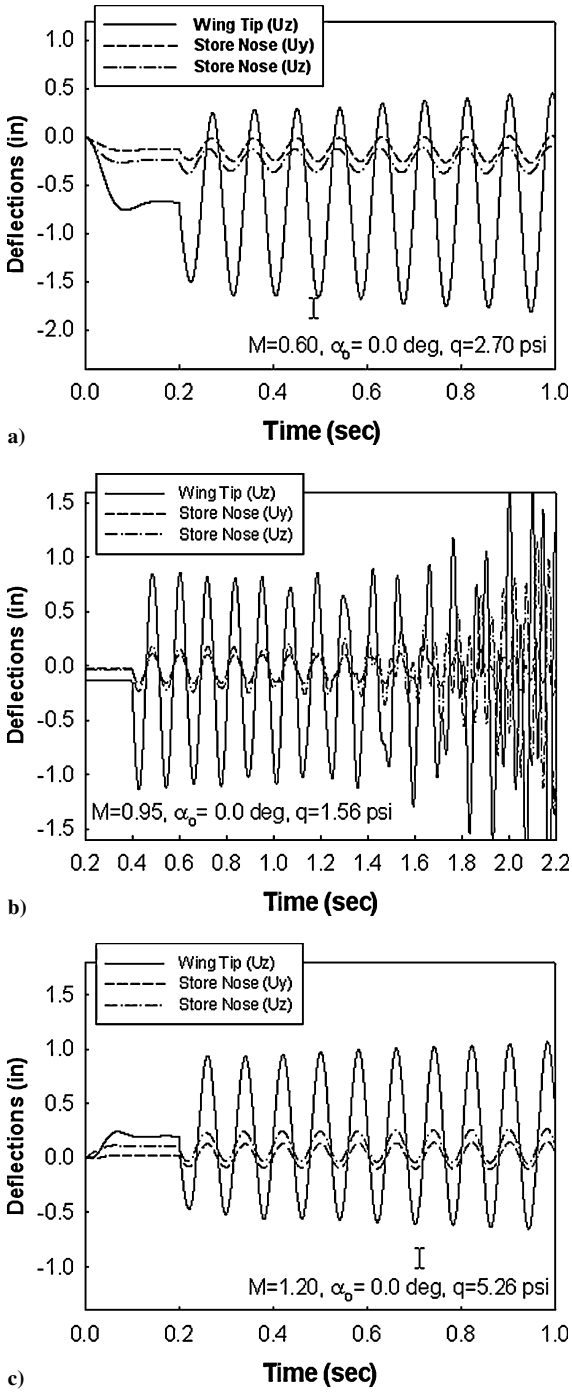

Fig. 12 Physical aeroelastic responses at the wing tip and the store nose: a) $M = 0.6$, b) $M = 0.95$, and c) $M = 1.2$.

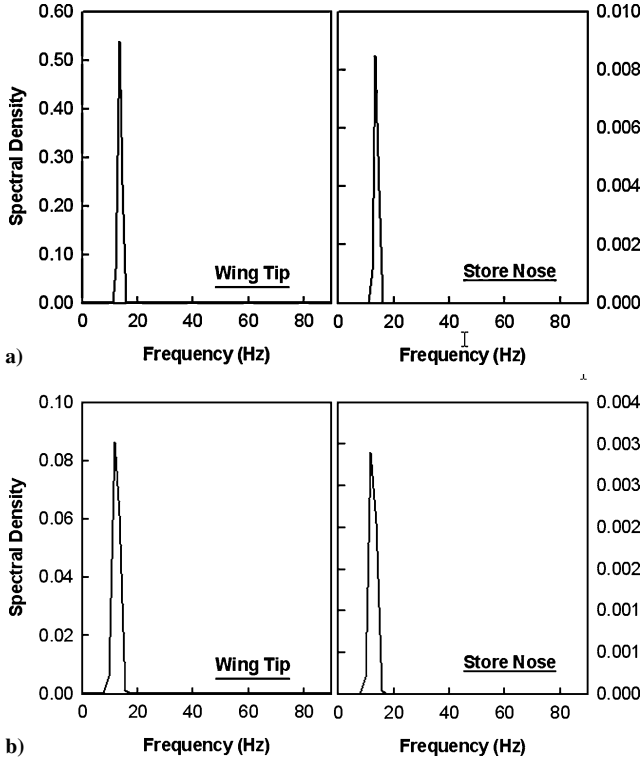

Fig. 13 Autospectral density functions for responses at wing tip and store nose: a) $M = 0.6$, $q = 2.70$ psi and b) $M = 1.2$, $q = 5.26$ psi.

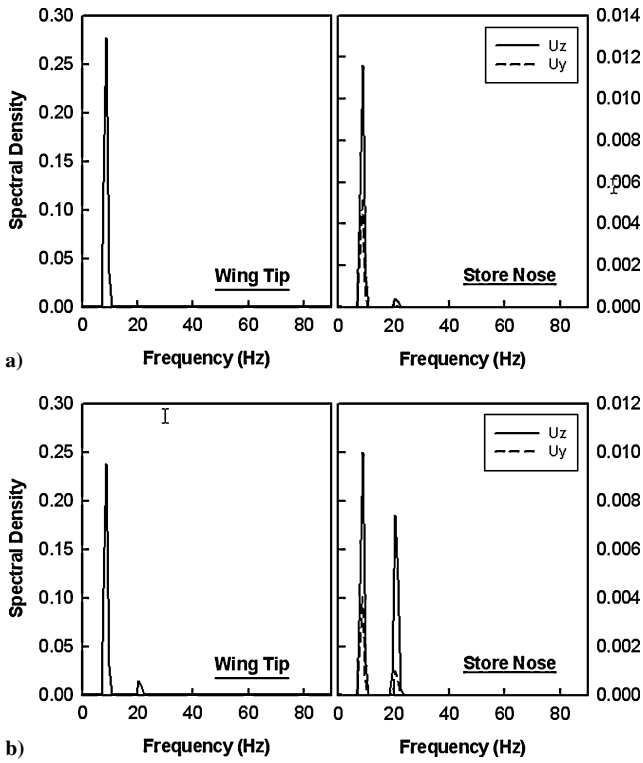

Fig. 14 Autospectral density functions for responses at wing tip and store nose; $M = 0.95$: a) $t = 0.4$–1.1 s and b) $t = 1.1$–2.0 s.

and the store nose. However, for $M = 0.95$, there are two different flutter frequencies, as shown in Fig. 14. Especially, for the latter-half of responses at the store nose, the unusual combination of two different frequencies in both pitch and yaw directions are shown. The second peak in Fig. 14b indicates the independent store dominant frequency, which is also close to the second natural vibration frequency.

Finally, the comparison of normalized flutter dynamic pressures is presented in Fig. 15. Here, the flutter dynamic pressure is normalized by the reference value of Mach 0.6. For the results using linear aerodynamic theories, the aerodynamic effects of pylon and store are not considered in the aerodynamic model. The two different approaches show similar trends at Mach 0.6 and over Mach 1.2. This also gives a preview for the present model that the aerodynamic interference effects of the pylon/store may be negligible for these Mach numbers. However, for the transonic region, such as Mach 0.9 and 0.95, the situation is very different, and a typical transonic dip phenomenon is shown. The CFD-based advanced flutter computations considering the accurate aerodynamic shape of the pylon and finned-store with shock wave effects gives much more conservative data than those predicted by classical linear aerodynamic theory.

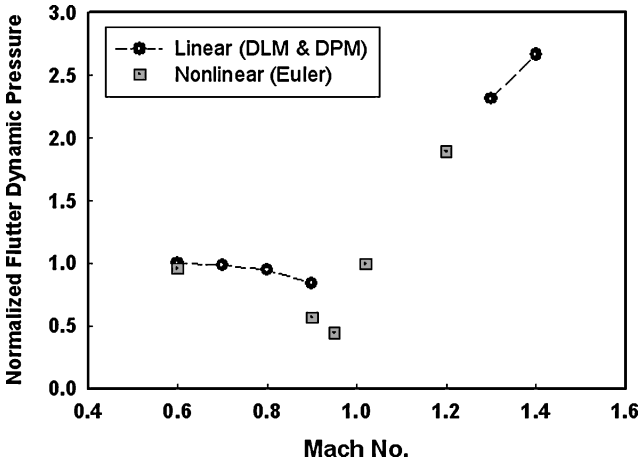

Fig. 15 Comparison of normalized flutter dynamic pressures.

Conclusions

We have developed a general computational aeroelastic analysis system coupled with advanced numerical technologies such as CFD/CSD and high-speed parallel processing. The robust numerical computation of the unstructured grid system has been successfully applied to a complex configuration of a wing with pylon/finned-store. A matched-point concept using standard atmosphere is applied to yield a physically meaningful solution for the actual flow conditions. With use of the developed analysis system, the nonlinear static and dynamic aeroelastic behavior of a wing with pylon/finned-store was investigated and simulated in the transonic and low-supersonic flow regions. From the present computational results, it is typically shown that the advanced numerical approach yields a much more conservative flutter boundary for a wing/store model than those of classical linear aerodynamic theories in high transonic flow. The aerodynamic interference effect of the pylon/store for the present model seems to be negligible in the low subsonic flow region, such as Mach 0.6. For transonic flow, an important result is that critical nonlinear flutter or limit-cycle oscillationlike phenomena tend to be dominantly induced by, or within the bounds of strong possibility due to, the shock coupling effect of unstable store induced vibration. In addition, for transonic flow, it is shown that there can be unusual transition phenomenon with different frequencies under the flutter vibration conditions of the wing with pylon/finned-store.

Acknowledgments

This work was partially supported by the Brain Korea 21/NURI Project, Research Center of Aircraft Part Technology, and the National Research Laboratory Program (2000-N-NL-01-C250) of the Korea Ministry of Science and Technology.

References

[1]Borland, C. J., and Rizzetta, D. P., "Nonlinear Transonic Flutter Analysis," *AIAA Journal*, Vol. 20, No. 11, 1982, pp. 1606–1615.

[2]Guruswamy, G. P., and Goorjian, P. M., "Unsteady Transonic Aerodynamics and Aeroelastic Calculations at Low-Supersonic Freestreams," *Journal of Aircraft*, Vol. 25, No. 10, 1988, pp. 955–961.

[3]Bennett, R. M., Batina, J. T., and Cunningham, H. J., "Wing-Flutter Calculations with the CAP-TSD Unsteady Transonic Small-Disturbance Program," *Journal of Aircraft*, Vol. 26, No. 9, 1989, pp. 876–882.

[4]Rausch, R. D., Batina, J. T., and Yang, H. T. Y., "Three-Dimensional Time-Marching Aeroelastic Analyses Using an Unstructured-Grid Euler Method," *AIAA Journal*, Vol. 31, No. 9, 1993, pp. 1626–1632.

[5]Lee-Rausch, E. M., and Batina, J. T., "Wing Flutter Boundary Prediction Using Unsteady Euler Aerodynamic Method," *Journal of Aircraft*, Vol. 32, No. 2, 1995, pp. 416–422.

[6]Lee-Rausch, E. M., and Batina, J. T., "Wing Flutter Computations Using an Aerodynamic Model Based on the Navier–Stokes Equations," *Journal of Aircraft*, Vol. 33, No. 6, 1996, pp. 1139–1147.

[7]Gupta, K. K., "Development of a Finite Element Aeroelastic Analysis Capability," *Journal of Aircraft*, Vol. 33, No. 5, 1996, pp. 995–1002.

[8]Koobus, B., and Farhat, C., "Second-Order Implicit Schemes that Satisfy the GCL for Flow Computations on Dynamic Grids," AIAA Paper 98-113, Jan. 1998.

[9]Alonso, J. J., and Jameson, A., "Fully-Implicit Time-Marching Aeroelastic Solutions," AIAA Paper 94-0056, 1994.

[10]Farhat, C., Lesoinne, M., Chen, P. S., and Lanteri, S., "Parallel Heterogeneous Algorithms for the Solution of Three-Dimensional Transient Coupled Aeroelastic Problems," AIAA Paper 95-1290, 1995.

[11]Byun, C., and Guruswamy, G. P., "Aeroelastic Computations on Wing-Body-Control Configurations on Parallel Computers," *Journal of Aircraft*, Vol. 35, No. 2, 1998, pp. 288–294.

[12]Goodwin, S. A., Weed, R. A., Sankar, L. N., and Raj, P., "Toward Cost-Effective Aeroelastic Analysis on Advanced Parallel Computing Systems," *Journal of Aircraft*, Vol. 36, No. 4, 1999, pp. 710–715.

[13]Liu, F., Cai, J., Zhu, Y., Wong, A. S. F., and Tsai, H. M., "Calculation of Wing Flutter by a Coupled CFD–CSD Method," AIAA Paper 2000-0907, Jan. 2000.

[14]Bohbot, J., Garnier, J., Toumit, S., and Darracq, D., "Computation of the Flutter Boundary of an Airfoil with a Parallel Navier–Stokes Solver," AIAA Paper 2001-0572, Jan. 2001.

[15]Melville, R., "Nonlinear Simulation of F-16 Aeroelastic Instability," AIAA Paper 2001-0570, Jan. 2001.

[16]Pollock, S. J., Sotomayer, W. A., Huttsell, L. J., and Cooley, D. E., "Evaluation of Methods for Prediction and Prevention of Wing/Store Flutter," *Journal of Aircraft*, Vol. 19, No. 6, 1982, pp. 492–498.

[17]Triplett, W. E., "Wind Tunnel Correlation Study of Aerodynamic Modeling for F/A-18 Wing-Store Tip-Missile Flutter," *Journal of Aircraft*, Vol. 21, No. 5, 1984, pp. 329–334.

[18]Guruswamy, G. P., Goorjian, P. M., and Tu, E. L., "Transonic Aeroelasticity of Wings with Tip Stores," *Journal of Aircraft*, Vol. 24, No. 10, 1987, pp. 688–695.

[19]Gern, F. H., and Librescu, L., "Static and Dynamic Aeroelasticity Wings Carrying External Stores," *AIAA Journal*, Vol. 36, No. 7, 1998, pp. 1121–1129.

[20]Kim, D. H., and Lee, I., "Transonic and Low-Supersonic Aerodynamic Analysis of a Wing with Underpylon/Store," *Journal of Aircraft*, Vol. 37, No. 1, 2000, pp. 189–192.

[21]Kim, D. H., and Lee, I., "Transonic and Supersonic Flutter Characteristics of a Wing-Box Model with Tip Stores," AIAA Paper 2001-1464, April 2001.

[22]Park, Y. M., and Kwon, O. J., "Unsteady Flow Computations Using a 3-D Parallel Unstructured Dynamic Mesh Adaptation Algorithm," AIAA Paper 2001-0865, Jan. 2001.

[23]Roe, P. L., "Approximate Riemann Solvers, Parameter Vectors and Difference Schemes," *Journal of Computational Physics*, Vol. 43, 1981, pp. 357–372.

[24]Bruner, C., "Parallelizations of the Euler Equations on Unstructured Grids," Ph.D. Dissertation, Dept. of Aerospace Engineering, Virginia Polytechnic Inst. and State Univ., Blacksburg, VA, 1996.

[25]Karypis, G., and Kumar, V., "Analysis of Multilevel Graph Partitioning," Dept. of Computer Science, Rept. TR 95-037, Univ. of Minnesota, 1995.

[26]Blom, F. J., "Considerations on the Spring Analogy," *International Journal for Numerical Methods in Fluids*, Vol. 32, 2000, pp. 647–668.

[27]Batina, J. T., "Unsteady Euler Airfoil Solutions Using Unstructured Dynamic Meshes," *AIAA Journal*, Vol. 28, No. 8, 1990, pp. 1381–1388.

[28]Pirzadeh, S. Z., "An Adaptive Unstructured Grid Method by Subdivision, Local Remeshing, and Grid Movement," AIAA Paper 99-3255, June–July 1999.

[29]Farhat, C., Pierson, K., and Degand, C., "CFD Based Simulation of the Unsteady Aeroelastic Responses of a Maneuvering Vehicle," AIAA Paper 2000-0899, Jan. 2000.

[30]Kim, D. H., Park, Y.-M., and Lee, I., "Nonlinear Aeroelastic Computation of Wings with Pylon/Finned-Store Using Parallel Unstructured Euler Solver," AIAA Paper 2002-1289, April 2002.

[31]Appa, K., "Finite-Surface Spline," *Journal of Aircraft*, Vol. 36, No. 5, 1989, pp. 495–496.

[32]Smith, M. J., Cesnik, C. E. S., Hodges, D. H., and Moran, K. J., "An Evaluation of Computational Algorithms to Interface between CFD and CSD Methodologies," AIAA Paper 96-1400, April 1996.

[33]Kim, D. H., and Lee, I., "CFD-Based Matched-Point Transonic and Supersonic Flutter Computations Using a Modified TSD Equation," *Computational Fluid Dynamics Journal*, Vol. 11, No. 1, 2002, pp. 35–49.

K. Ghia
Associate Editor